frontiers | Frontiers in Earth Science

ORIGINAL RESEARCH
published: 04 August 2022
doi: 10.3389/feart.2022.889268

Distinctive Sedimentary Evolution at the East Edge of the Central Yellow Sea Mud Over the Past 45 kyr: Evidence From Detrital Mineralogy

Yao Zhang[1,2,3], *Xianwei Meng*[2]*, *Zongzhu Han*[3]*, *Bingfu Jin*[4], *Zhiqing Lai*[3] and *Jinqing Liu*[5]

[1]Qingdao Institute of Marine Geology, China Geologic Survey, Qingdao, China, [2]First Institute of Oceanography, Ministry of Natural Resources, Qingdao, China, [3]College of Marine Geosciences, Ocean University of China, Qingdao, China, [4]School of Resources and Environmental Engineering, Ludong University, Yantai, China, [5]College of Earth Science and Engineering, Shandong University of Science and Technology, Qingdao, China

The central Yellow Sea Mud (CYSM) is a vital part of the coastal sand and distal mud depositional system in the South Yellow Sea (SYS). Previous studies concerning the sedimentary evolution of this area have almost exclusively concentrated on its interior during the Holocene instead of its periphery. In this study, we used a sediment core (H10), with a significantly slow sedimentary rate, to reconstruct the sedimentary evolution at the east edge of the CYSM since MIS3a (~45 kyr). This mainly involved using detrital minerals, the chemical compositions of garnet, and grain size. The provenance of coarser sediments has remarkable Yellow River-derived characteristics, especially during MIS2 and MIS1. The sedimentary evolution was primarily controlled by hydrodynamic regimes accompanied by changes in relative sea levels (RSLs) and climates. During MIS3a, frequent RSL fluctuations and powerful tidal current erosion were responsible for two facie shifts from the neritic sea to the shore and the lower sedimentary rate in the study area. A paleo-cold water mass and muddy deposition occurred during the high RSL stages with authigenic pyrite enrichment. During MIS2, the paleo-Yellow River was distributed on the SYS and flowed through the study area. Fluvial deposition on the shelf may be eroded by the strong winter monsoon, with an extremely dry and cold climate. Since ~9.6 kyr, intense hydrodynamic regimes, which were induced by tidal current and upwelling, were responsible for the very much thin deposition, and coarser sediments remained in the study area. Notably, combined with previously studied cores, a much more detailed and intuitional cognition for CYSM formation can be obtained *via* our special perspective: mud periphery. This study elucidates the sedimentary system evolution and mud area formation of continental shelf seas.

Keywords: sedimentary evolution, provenance, central Yellow Sea Mud, detrital minerals, garnet

OPEN ACCESS

Edited by:
Daidu Fan,
Tongji University, China

Reviewed by:
Zhongbo Wang,
Shantou University, China
Selvaraj Kandasamy,
Xiamen University, China

***Correspondence:**
Xianwei Meng
mxw@fio.org.cn
Zongzhu Han
hanzongzhu@ouc.edu.cn

Specialty section:
This article was submitted to Quaternary Science, Geomorphology and Paleoenvironment, a section of the journal Frontiers in Earth Science

Received: *04 March 2022*
Accepted: *26 May 2022*
Published: *04 August 2022*

Citation:
Zhang Y, Meng X, Han Z, Jin B, Lai Z and Liu J (2022) Distinctive Sedimentary Evolution at the East Edge of the Central Yellow Sea Mud Over the Past 45 kyr: Evidence From Detrital Mineralogy. Front. Earth Sci. 10:889268. doi: 10.3389/feart.2022.889268

1 INTRODUCTION

The South Yellow Sea (SYS), a typical semi-enclosed epicontinental sea of the western Pacific, has an area of 3.09×10^5 km^2, with an average water depth of 46 m and a maximum water depth of 140 m and is surrounded by the Chinese mainland and Korean peninsula (**Figure 1**; Qin et al., 1989). As one of the broadest continental shelf units in the world, the SYS receives abundant terrestrial sediments on its gentle slope and is characterized by its complex geomorphology, varied sedimentary

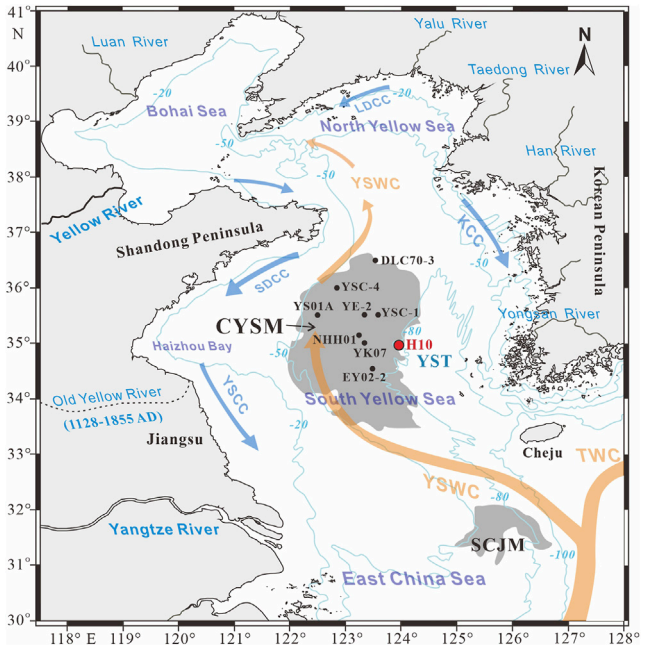

FIGURE 1 | Locations of sediment cores in the central Yellow Sea mud (CYSM) (**Supplementary Table S1**, modified from Wang et al., 2014b; new core H10 is marked by a red dot) and regional circulation pattern (modified from Li et al., 2016). The orange lines indicate warm current systems, whereas blue lines indicate cold coastal currents. YSWC, Yellow Sea Warm Current; TWC, Tsushima Warm Current; YSCC, Yellow Sea Coastal Current; KCC, Korean Coastal Current; SDCC, Shandong Coastal Current; LDCC, Liaodong Coastal Current; YST, Yellow Sea Trough; and SCJM, southwest Cheju Island mud.

environment, intricate ocean current patterns, and diverse marine organisms (Qin et al., 1989; Yang et al., 2003; Gao and Collins, 2014; Li et al., 2016). Under changes in relative sea-level (RSL), climate, and ocean environment, both the sediment supply from multiple sources and hydrodynamic conditions of the SYS varied remarkably during the late Quaternary. This gave rise to region-specific evolution of the sedimentary environment, thereby promoting the formation of a complicated coastal sand and distal mud depositional system in the Holocene. This system includes sandy deposits in Haizhou Bay, tidal sand ridges off the Jiangsu and Korean coasts, silty submerged deltas off the Shandong peninsula and old Yellow River mouth, and muddy patches in the central Yellow Sea and the coast of the Korean peninsula (Shi et al., 2012; Gao and Collins, 2014). Therefore, studies on the late Quaternary evolution of the sedimentary environment of this system in the SYS have never ceased, especially on the Central Yellow Sea Mud (CYSM) (**Figure 1**; Alexander et al., 1991; Park et al., 2000; Liu et al., 2002, Liu et al., 2004; Yang and Liu, 2007; Yang and Youn, 2007; Xiang et al., 2008; Li et al., 2014b; Liu et al., 2014a; Lim et al., 2015; Mei et al., 2016; Hu et al., 2018). The CYSM comprises the largest mud patch on the East China continental shelf and contains abundant information regarding the sea level and climate change, terrestrial sediment supply, hydrodynamic regime, and paleo-environmental evolution.

However, the majority of researchers have reconstructed the sedimentary evolution of the CYSM during the Holocene, using the records of clay minerals, magnetics, and the element and isotope geochemistry of fine sediments from the interior of the CYSM (Park et al., 2000; Xiang et al., 2008; Li et al., 2014b; Lim et al., 2015; Hu et al., 2018). Few studies have focused on the sedimentary evolution at the periphery of the CYSM, which is important not only for enriching our knowledge of the sedimentary evolution of the coastal sand and distal mud deposit system of the marginal sea but also for systematically understanding the formation process and mechanism of the mud area.

Clarifying sediments provenance is the precondition and requirement to explicating sedimentary evolution (Morton and Hallsworth, 1994; Huang et al., 2019). Detrital mineral composition and distribution patterns are significant not only for provenance studies (Morton and Hallsworth, 1994) but also for indicating transport processes, hydrodynamic conditions, stratigraphic correlations, sedimentary characteristics, and changes in RSL (Morton and Hallsworth, 1999; Sevastjanova et al., 2012). In particular, authigenic minerals have specific functions to indicate their sedimentary environment (Mange and Morton, 2007; Chen, 2008). In general, provenance signals recorded in detrital minerals can be altered by weathering, hydrodynamic sorting, mechanical breakdown, and burial-diagenesis (Mange and Maurer, 1992; Morton and Hallsworth, 1999; Garzanti et al., 2008). However, the ratio of detrital minerals with similar morphology, specific gravity, and other properties remains essentially invariable under complex hydrodynamic effects, long-distance transport, and weathering erosion. This largely eliminates the influence of non-physical factors and reflects the provenance information more realistically. Moreover, single-mineral geochemistry has proven to be a particularly useful tool in provenance analysis because it minimizes the effect of weathering and transport processes more in provenance studies compared to the tools of detrital mineral assemblage and ratio (Mange and Morton, 2007). Many single minerals, such as garnet, zircon, rutile, and amphibole, to mention a few, have been successfully used in provenance studies (Morton, 1985; Sabeen et al., 2002; Morton et al., 2004; Takeuchi et al., 2008; Krippner et al., 2014). Therefore, compared with traditional detrital mineral assemblage, choosing a reasonable detrital mineral ratio and a single mineral can effectively recover the provenance of sediments.

Here, a sediment core H10, which was collected from the east edge of the CYSM, was used to reconstruct the sedimentary evolution in this area over the past 45 kyr using data on detrital minerals, single-mineral geochemistry, and grain size. Compared with past relevant studies, this study encompasses several unusual features: 1) the sediment core H10, with a length of 216 cm and an age of 45 kyr, had a surprisingly low sediment rate (SR = 4.71 cm/kyr), a feature hardly reported in previous studies on the CYSM, 2) due to the long time span, we revealed the sedimentary evolution since the Marine Isotope Stage (MIS) 3a (not limited to the Holocene) and identified the existence of the paleo-Yellow River, 3) an original diagram of heavy mineral ratios and a classical garnet ternary diagram were used for provenance

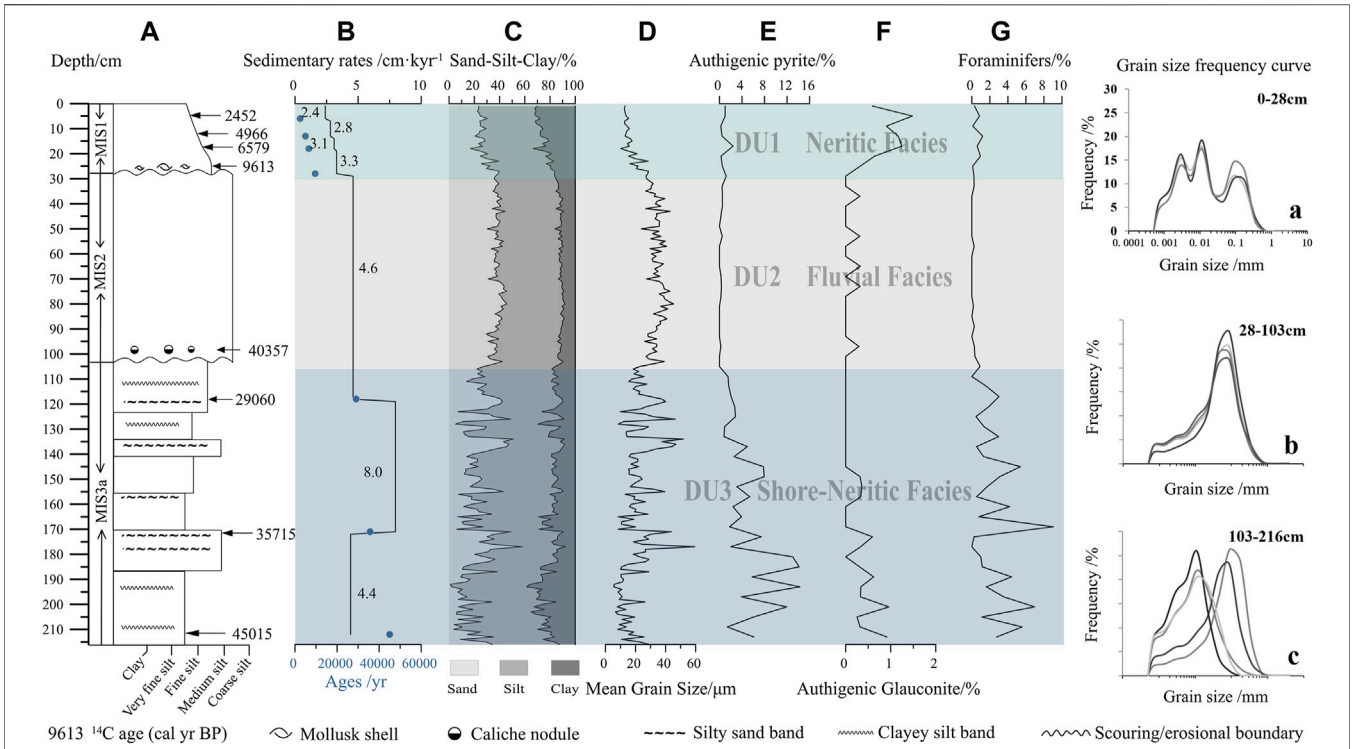

FIGURE 2 | Composite histogram of core H10 deposition **(A–G, a–c)**.

studies, which greatly reduced the influence of non-physical factors, and 4) using previous sedimentary records, this study provided a clear and intuitional cognition for the formation of the CYSM from a special perspective: mud periphery.

2 MATERIALS AND METHODS

2.1 Description of the Sediment Core

Sediment core H10, which has a length of 216 cm at a water depth of 81 m, was drilled near the west side of the Yellow Sea Trough (YST) bottom by a piston corer in 2016 (**Figure 1**). Coincidently, the core is located on the east edge of the CYSM (124°00′E, 35°00′N). According to the appearance of caliche nodules at the layer of 98–101 cm, fragmentized shells at 25–28 cm, and other sedimentary features, the core can be visually divided into three sections (**Figure 2A**): the lower section (216–103 cm) is characterized by dark gray sediments and plenty of clay–silt interbeds, the middle section (103–28 cm) contains dark yellowish-brown sandy sediments, and the upper section (28–0 cm) is mainly composed of yellowish-brown fine sediments and has a higher water concentration. Detailed identification of the shells verified that they belong to *Mya arenaria*, a kind of benthic shellfish that lives in a temperate zone, prefers to inhabit shallow coastal waters and is widely distributed in the Yellow Sea and Bohai Sea (Qin et al., 1989). In addition, the rough outer surfaces of the shells are covered by yellowish-brown skin (**Figure 3A**). The caliche nodules are yellowish-brown in appearance, gray on the interior, and lumpy in shape with a high psephicity (**Figure 3B**). The sediment sub-sampling intervals for grain size analysis and detrital mineral identification are 1 and 4 cm, respectively. Apart from measurements of the accelerator mass spectrometry (AMS) ^{14}C dating and stable carbon isotope ($\delta^{13}C$), other analyses were performed at the Key Lab of Submarine Geosciences and Exploring Technique, Ocean University of China.

2.2 AMS ^{14}C Dating and $\delta^{13}C$ Measurements

The shells of *M. arenaria*, caliche nodules, and fresh mixed-species benthic *Foraminifera* from three horizons were selected for AMS ^{14}C dating measurement by the Beta Analyses Company, United States (**Table 1**). After eliminating the effect of the regional carbon reservoir ($\Delta R = -81 \pm 60$), the conventional radiocarbon ages were corrected to calibrated calendar years by the program Calib 7.1 with Marine 13 calibration curves (Reimer et al., 2013). The calibrated age unit (cal. kyr BP) in this study is abbreviated as kyr. The values of $\delta^{13}C$ were analyzed by using a Thermo Scientific isotope ratio mass spectrometer, with a standard deviation of ±0.3‰ and can be used to identify the terrestrial and marine carbonate (Keith and Weber, 1964).

2.3 Grain Size Analysis

The grain size of 216 sub-samples was measured by using a Malvern Mastersizer 2000 laser particle analyzer (Malvern, Inc., United Kingdom) at a measurement range of 0.02–2000 μm and a size resolution of 0.01 φ. The procedure was as follows: 0.5–1 g of sediments were placed into 50 ml beakers, then pretreated with

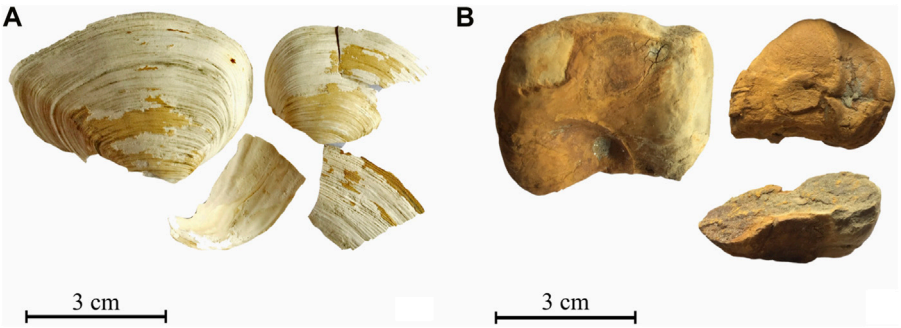

FIGURE 3 | Shells at 25–28 cm **(A)** and caliche nodules at 98–100 cm of **(B)** core H10.

TABLE 1 | AMS ^{14}C dating and stable carbon isotopic ($\delta^{13}C$) data of the H10 core.

Depth (cm)	Material	Conventional age (yr BP)	Calendar year (cal. yr BP)	$\delta^{13}C$ (‰)	Sedimentary rate (cm/kyr)
5–6	*Foraminifera*	2,610 ± 30 BP	2,452	−1.1	2.4
12–13	*Foraminifera*	4,610 ± 30 BP	4,966	0.3	2.8
17–18	*Foraminifera*	6,070 ± 30 BP	6,579	0.6	3.1
27–28	Shell	8,840 ± 30 BP	9,613	1.2	3.3
98–100	Caliche nodule	35,700 ± 310 BP	40,357	−12.2	
117–118	*Foraminifera*	25,350 ± 110 BP	29,060	0.3	4.6
170–171	*Foraminifera*	32,140 ± 210 BP	35,715	0.6	8.0
211–212	*Foraminifera*	41,940 ± 680 BP	45,015	0.1	4.4

5 ml 30% H_2O_2, and 15 ml 0.5 mol/L HCl for 24 h to remove organic matter and carbonate, respectively. After ultrasonic dispersion, the samples were tested by using an analyzer whose measuring error was within 3%.

2.4 Detrital Mineral Analysis

According to the grain size, 20–100 g of dried sediment was placed into a beaker with water added $(NaPO_3)_6$ to disperse the samples sufficiently. Subsequently, the very fine sand-sized fraction (63–125 μm) was extracted by wet sieving before it was dried and weighed. After using bromoform as a separation liquid (density 2.89 g/cm^3), the light and heavy minerals were collected and weighed. The identification of detrital minerals was carried out under an Olympus SZ61 stereomicroscope and SZX51 polarizing microscope through the oil immersion method, microchemistry experiment, and electron probe analysis. According to the ribbon method, 54 sub-samples were identified (Galehouse, 1971). More than 300 light mineral particles and 400 heavy mineral particles were counted for each sample, and the grain percentage (%) of each mineral species was calculated.

2.5 Chemical and End-Member Compositions of Garnets

A total of 32, 44, 32, 73, 68, and 56 garnet grains in the layers 8–9 cm, 48–49 cm, 84–85 cm, 132–133 cm, 172–173 cm, and 212–213 cm, respectively, were selected and analyzed using a JXA-8230 electron probe with silicate and oxide standard samples from the SPI Company, United States. The test conditions were as follows: 15 KV acceleration voltage, 20 nA probe current, and 20 s test time for various elements. The experimental accuracy of major elements was better than 1%, and that of trace elements was better than 5%.

Garnet, a group of cubic nesosilicate minerals, has 14 end-member compositions altogether (Grew et al., 2013). The most common end-member species are almandine, pyrope, spessartine, and grossular. Natural garnet generally consists of a solid solution of these end-members in highly varying proportions (Krippner et al., 2014). According to the weight percentage of each oxide in garnet (the value of Fe_2O_3 is calculated by charge balance) and coordination numbers of oxygen atoms (cation coefficient calculated by 12 oxygen atoms), the end-member compositions of each garnet grain and their percentages were calculated.

3 RESULTS

3.1 Chronology and Sedimentary Rates

The results of the conventional radiocarbon ages, calibrated calendar years, and $\delta^{13}C$ for eight samples are listed in **Table 1**. The caliche nodule has very negative $\delta^{13}C$

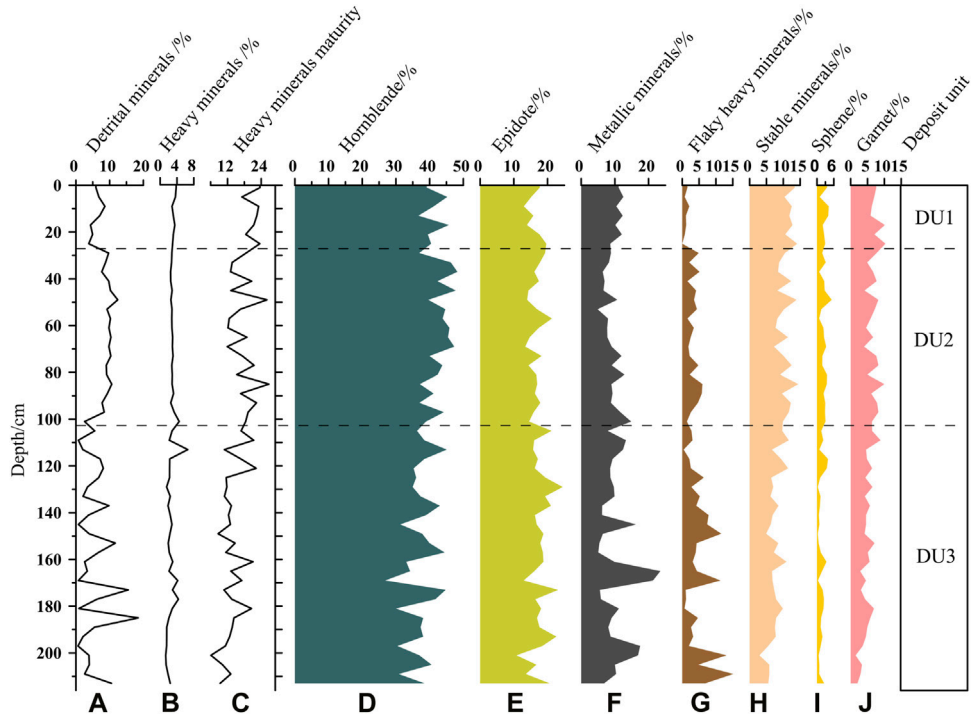

FIGURE 4 | Depth *versus* major heavy minerals content **(A–J)** in core H10 (detailed data in **Supplementary Table S2**).

(−12.2‰), which indicates that the nodule is formed under freshwater conditions (Keith and Weber, 1964), and likely inherited features from ancient terrestrial materials. Therefore, its age (~40 kyr) should be omitted. Conversely, the ages of one shell and six foraminifer samples are effective to establish the chronological framework. Hence, the SRs of 212–171, 171–118, 118–28, 28–19, 19–14, 14–7, and 7–0 cm layers are 4.4, 8.0, 4.6, 3.3, 3.1, 2.8, and 2.4 cm/kyr, respectively (**Figure 2B**).

The entire core, which has a length of 216 cm, was determined to be 45 kyr, giving it the low average SR of 4.7 cm/kyr. Particularly, the averaged SR of 2.9 cm/kyr in the Holocene is significantly slower than those sites lying in the inner and west regions of the CYSM (**Figure 1**; **Supplementary Table S1**), such as 114.5 cm/kyr for core YS01A (Wang et al., 2014b), 73.2 cm/kyr for core YE-2 (Xiang et al., 2008), 54.2 cm/kyr for core YSC-4 (Li et al., 2014b), 50.2 cm/kyr for core YSC-1 (Hu et al., 2018), 44.1 cm/kyr for core NHH01 (Liu et al., 2014a), 36.5 cm/kyr for core YK07 (Alexander et al., 1991), and 13.3 cm/kyr for core EY02-2 (Zhuang et al., 2002).

3.2 Variations of Grain Size and Deposit Units

The mean grain size (Mz) of the H10 core varies acutely, ranging from 5.6 to 59.5 μm, with an average value of 25.0 μm. According to the vertical variation of the grain size (**Figures 2C,D**) and its lithological characteristics (**Figure 2A**), the core can be divided into three deposit units (DU): DU3 (216–103 cm), DU2 (103–28 cm), and DU1 (28–0 cm). The average Mz of DU3, DU2, and DU1 are 20.8, 34.2 μm, and 17.4 μm with features of dramatic fluctuation, relative stabilization, and gradually diminution, respectively (**Figure 2C**). The proportions of sand, silt, and clay in DU3 are 22.8, 58.4, and 18.8%, respectively. In DU2, they are 38.2, 50.2, and 11.6%, and in DU1, they are 27.7, 47.7, and 24.6%, respectively (**Figure 2B**). The vertical variations of the three fractions in each section are similar to their Mz. Moreover, the typical grain size frequency curves are characterized by diverse non-normal unimodal curves in DU3, uniform remarkable unimodal curves in DU2, and similar multimodal curves in DU1 (**Figures 2A–C**).

3.3 Variations of Detrital Minerals

The content of detrital minerals (i.e., very fine sand fraction of 63–125 μm) is 6.8% on average, ranging from 0.6 to 18.5%, with a variation similar to the grain size (**Figures 2C,D**, **4A**). There are more than 40 kinds of heavy minerals, even though their proportion reaches as low as 2.7%, with fluctuating change (**Figure 4B**). In this study, we focused on heavy minerals, authigenic minerals, and *Foraminifera*. Heavy minerals mainly include those that have potential implications for sedimentary facies, hydrodynamic conditions, and sediment provenance.

3.3.1 Major Heavy Minerals

Both hornblende and epidote are the primary species of unstable heavy minerals, and their average contents are 39.6 and 17.2%, ranging from 26.8 to 48.2% and from 10.8 to 24.5%, respectively (**Figures 4D,E**).

Metallic minerals, except for authigenic pyrite, include ilmenite, magnetite, limonite, hematite, and leucoxene. Their average content is 10.0%, ranging from 4.9 to 23.5% (**Figure 4F**).

The flake heavy minerals are mainly composed of flaky biotite, muscovite, and weathered mica, with the exception of the occasional appearance of thick-plate biotite. Their content is 3.9% on average with a large range of 0%–15.1% and exhibits an undulating descent, which is characterized by a higher average value of 5% in DU3, followed by 3.3% in DU2, and 1.5% in DU1, with dramatic, moderate, and slight fluctuation, respectively (**Figure 4G**).

Stable minerals mainly include garnet, sphene, apatite, tourmaline, and zircon. Their average content is 9.1%, with a range of 2.9%–14.4%. Among the stable minerals in the H10 core, sphene and garnet are the primary species, accounting for 5.8 and 2.1% of total heavy minerals on average, respectively. Their changes in content are noted, which is increasing gradually from bottom to top (**Figures 4H–J**).

The heavy mineral maturity, which is the ratio of stable minerals to unstable minerals, is widely used to reflect the weathering degree and transporting distance of minerals from source to sink. From bottom to top, its value gradually increases with a mean value of 16.1 (**Figure 4C**).

3.3.2 Authigenic Minerals and Foraminifer

The authigenic pyrite, authigenic glauconite, and foraminifer exhibit three-stages of variation (**Figures 2E–G**), which correspond to the variations in sedimentary characteristics and grain size (**Figures 2A,C,D**).

The content of authigenic pyrite varies from 0 to 14.3%, with an average of 2.8%. It is significantly more abundant in the DU3 than in DU2 and DU1. The content of this mineral in DU3 presents an acutely fluctuant decrease with an average value of 2.80%. Conversely, DU1 contains barely 0.82%, and it is nearly absent in DU2 (**Figure 2E**).

Authigenic glauconite, which belongs to light mineral, mainly appears in DU3 and DU1, exhibiting a gentle decrease to disappearance and an abrupt increase in its content, with average values of 0.22 and 0.80%, respectively. Meanwhile, in DU2, this mineral almost disappears, and only occasionally exists in some horizons with much lower proportions (**Figure 2F**).

The *Foraminifera* content varies from 0 to 9.03%, with an average of 1.35%. These values are calculated by the percentage of the number of *Foraminifera* particles in the total number of detrital minerals particles. It is relatively abundant and fluctuates remarkably in DU3 with an average content of 2.45%, whereas it is as low as 0.54% in DU1 and almost disappears in DU2 (**Figure 2G**).

3.4 End-Member Compositions of Garnet

The garnet herein, commonly composed of almandine, pyrope, spessartine, and grossular in end-member compositions, generally exhibits a two-stage variation from 216 to 103 cm to the surface (**Figure 5A**). The average proportions of these four end-member compositions for the entire sediment core are 68.2, 22.9, 5.7, and 3.3 mol%, respectively, as calculated by the analyzed chemical compositions, which mainly included SiO_2, FeO, Al_2O_3, MgO, CaO, MnO, TiO_2, and Cr_2O_3 (**Supplementary Table S3**). The average proportions of almandine at six layers are approximately equal to each other, with a narrow range of 67.3%–69.0%. Conversely, the averaged proportions of pyrope, grossular, and spessartine across the six layers varied obviously, with ranges of 20.7%–25.0%, 3.9%–8.3%, and 2.5%–4.2%, respectively (**Figures 5B,C**).

4 DISCUSSION

4.1 Provenance Evolution of Detrital Minerals

4.1.1 Potential Sources of the Sediment in the SYS

In general, the potential sources of sediments from the central SYS include the Yellow River, Yangtze River, small rivers in the Korean and Shandong peninsulas, and eroded products from the coasts and seabed. Previous research has demonstrated that the Yangtze River and the Yellow River are the predominant sediment contributors to the central SYS (Milliman et al., 1985, Milliman et al., 1987; Alexander et al., 1991; Park et al., 2000; Liu et al., 2002; Yang et al., 2003; Yang and Liu, 2007; Yang and Youn, 2007), and even for the previously deposited and afterward eroded sediments on the seabed (Qin et al., 2018). The sediment supplies from the smaller rivers in the Korean Peninsula are only deposited, however, to the east of 125°E of the SYS under the action of the Korean coastal current (Cho et al., 1999). Recent studies proved that the eroded materials along the coasts and outputs from the smaller rivers in Shandong peninsula are probably the additional contributors to the SYS (Liu et al., 2017, Liu et al., 2022). Thus, the materials from the Yellow River, Yangtze River, and Shandong peninsula can be reasonably considered to be the potential sources of the sediments in core H10.

4.1.2 Qualitative Discrimination of Provenances Using Heavy Mineral Ratios

As previously mentioned, detrital mineral ratios are a more effective method for provenance discrimination. The Yellow River is characterized by more hornblende and garnet, while the Yangtze River contains more epidote and sphene (Wang et al., 2007; Jin et al., 2019). There are similar qualities between hornblende and epidote, as well as garnet and sphene. Thus, the garnet/sphene–hornblende/epidote (GS-HE) diagram can be established as a new method for provenance discrimination.

The GS–HE diagram shows that the DU1 and DU2 dots are both from the Yellow River range, wherein the latter is closer to the Yellow River than the former. Meanwhile, the DU3 dots display a wide distribution, most of which signal a nearness to the

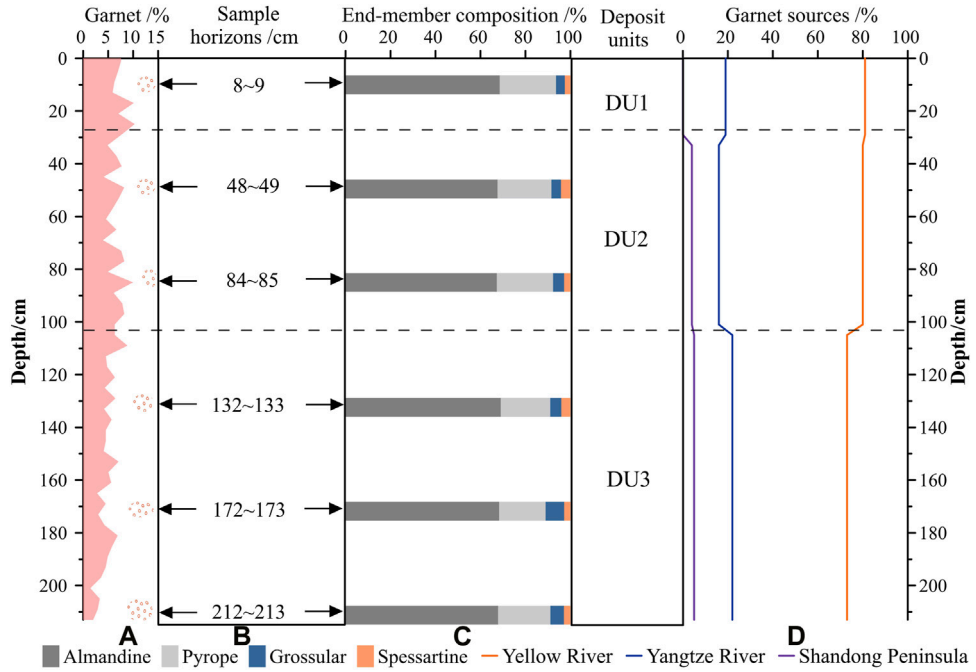

FIGURE 5 | End-member compositions of garnet at six horizons **(A–C)** of core H10 and the relative contributions of garnet sources **(D)** in different sedimentary deposit units.

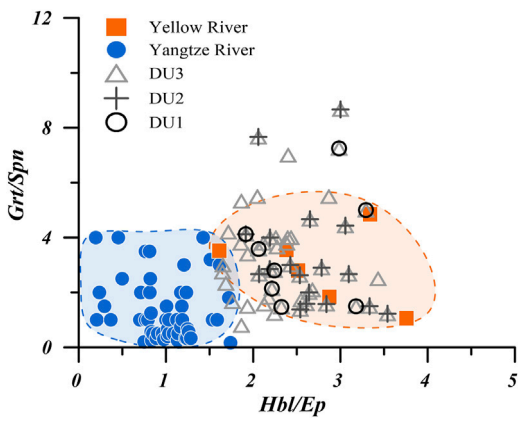

FIGURE 6 | GS–HE provenance discrimination diagram of core H10. Data regarding the Yellow River and Yangtze River are from Jin et al. (2019) and Wang et al. (2007), respectively. GS, garnet/sphene (Grt/Spm); HE, hornblende/epidote (Hbl/Ep).

Yellow River, and some of which are between the Yangtze River and Yellow River (**Figure 6**). Therefore, the source of detrital minerals in DU3 is determined to be greatly affected by the Yellow River but is also mixed with some of the Yangtze River's materials, while the provenance in DU2 and DU1 is mainly controlled by the Yellow River. In addition, the heavy mineral assemblage in DU2 is very similar to loess (He et al., 1997), and ~90% of the Yellow River sediments are derived from the Loess Plateau (Ren and Shi, 1986), which further confirms the irreplaceable contribution of the Yellow River in DU2.

4.1.3 Semi-Quantitative Discrimination of Provenances Using End-Member Compositions of Garnet

Single-mineral geochemistry has proven to be a particularly useful tool in provenance analysis (Mange and Morton, 2007). In particular, garnet, which is controlled by provenance from source to sink, is an ideal choice for provenance tracking (Morton, 1985; Sabeen et al., 2002; Morton et al., 2004; Takeuchi et al., 2008; Krippner et al., 2014) owing to various advantages: 1) as a granular stable heavy mineral, garnet is widely distributed in sediments; 2) it has different assemblage characteristics in different protoliths due to extensive isomorphism (Morton et al., 2004; Mange and Morton, 2007); and 3) unlike zircon and other minerals, its chemical compositions from the core to edge are relatively stable (Morton, 1987), making the test results uniform and objective.

The garnet G–P–AS ternary diagram established by grossular (G), pyrope (P), and almandine and spessartine (AS), can be used to discriminate sediment provenances effectively (**Figure 7S0**; Mange and Morton 2007; Krippner et al., 2014). Previous studies have concluded that the vast majority of the coarse materials discharged by the Yangtze River and Yellow River into the East China seas are separately supplied from the upper reach and middle reach with the Chinese Loess Plateau, not the lower reaches (Yang, 1988; Huang et al., 2019). Therefore, the end-member compositions of garnet derived from the upper reach of the Yangtze River, the middle reach of the Yellow River (Wang,

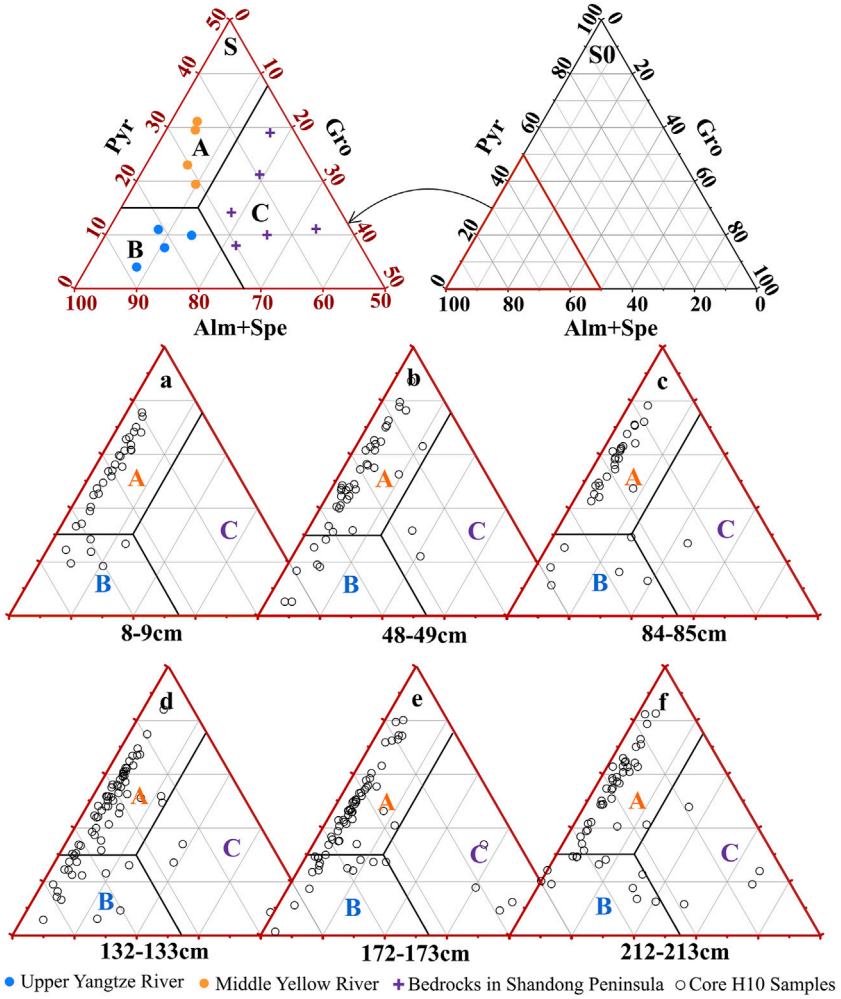

FIGURE 7 | Garnet G–P–AS ternary diagram (s0) for the upper Yangtze River, middle Yellow River (Wang, 2014), bedrock in the Shandong Peninsula (s, Liu et al., 2010b), and core H10 **(A–F)**. A, B, and C represent the provenance areas of the Yellow River, Yangtze River, and Shandong peninsula, respectively. G, grossular (Gro); P, pyrope (Pyr); A, almandine (Alm); and S, spessartine (Spe).

2014), and bedrocks of Shandong peninsula (Liu et al., 2010b) could represent the three provenance end-members of the Yangtze River, Yellow River, and Shandong peninsula in the ternary diagram, respectively. Because the end-member compositions of the garnet in the three provenance end-members are remarkably different, the diagram can be divided into three parts, wherein each represents a different source area as follows: (A) Yellow River, (B) Yangtze River, and (C) Shandong peninsula (**Figure 7S**).

In the G–P–AS ternary diagram (**Figures 7A–F**), the dots of the six horizons fall into area A, accounting for 81, 80, 80, 74, 72, and 73% of the dots at the horizons of 8–9, 48–49, 84–85, 132–133, 172–173, and 212–213 cm, respectively, with an overall average of 77%. Meanwhile, the proportions of the dots falling into area B at each horizon are 19, 16, 16, 22, 22, and 21%, respectively, with an average value of 19%, and the proportions of the dots falling into area C separately account for 0, 4, 3, 4, 6, and 6% of each horizon, with an average value of 4%. Based on these results and the positions of the six horizons in the deposit units, the relative contributions of garnet sources from the Yellow River, Yangtze River, and Shandong peninsula can be roughly estimated as 81, 19, and 0% for DU1, 80, 16, and 4% for DU2, and 73, 22, and 5% for DU3, respectively (**Figure 5D**). It is demonstrated that the Yellow River and Yangtze River are separately the predominant and secondary coarse sediment contributors at the east edge of the CYSM, especially in the DU1 and DU2. However, the Yangtze River provides more materials in DU3, and Shandong peninsula could be regarded as a neglected source for the entire sediment core. These results are consistent with those from the heavy mineral ratios.

4.2 Discrimination to Sedimentary Facies and Hiatus

Authigenic pyrite prefers to form in relatively stable oceanic hydrodynamic environments that have greater water depth and

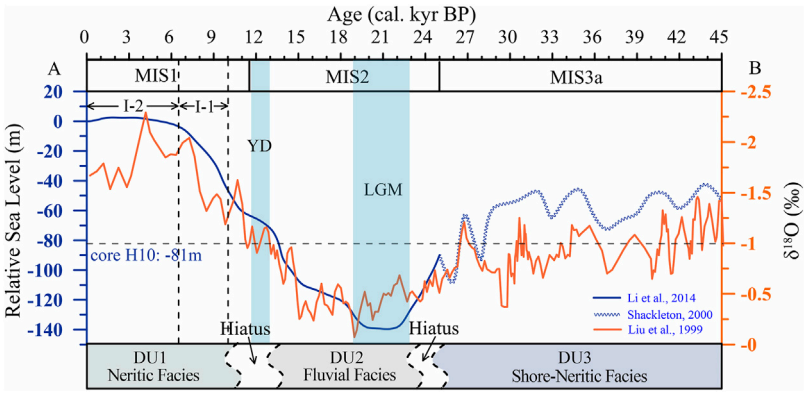

FIGURE 8 | Changes of the relative sea-level (RSL) **(A)** and oxygen isotope ($\delta^{18}O$) **(B)** since Marine Isotope Stage 3a (MIS3a).

reductive conditions, and authigenic glauconite is a typical mineral that forms in shallow seas with an oxidative environment (Morton and Hallsworth, 1994; Chen, 2008). Therefore, variations in these minerals, in combination with the grain size and *Foraminifera* content, can distinguish the sedimentary facies in each depositional unit.

In DU3, authigenic pyrite, authigenic glauconite, and foraminifer follow a fluctuating decline until they disappear (**Figures 2E–G**), and their variations approximately correspond with the fluctuation of the grain size with diverse grain size frequency curves (**Figures 2C,D**), which implies that there is an unstable sedimentary environment with two shifts from neritic to shore facies. Similarly, shore-neritic facies deposits are identified in core EY02-2 during the same period, with many clay–silt interbeds (Zhuang et al., 2002).

Both marine authigenic minerals and *Foraminifera* are nearly absent in DU2 (**Figures 2E–G**). The remarkable unimodal grain size frequency curves and favorable sorting collectively imply a strong and single hydrodynamic condition (**Figure 2B**). Moreover, the caliche nodules at 98–100 cm with good psephicity (**Table 1**; **Figures 2A**, **3B**), have a very negative $\delta^{13}C$, which coincides with the typical characteristics of freshwater carbonate. Therefore, this deposition unit is characterized by fluvial facies.

The DU1 contains some authigenic glauconite and a small number of pyrite and *Foraminifera*. Moreover, the $\delta^{13}C$ values of shell fragments and *Foraminifera* are more positive. These results show that this unit develops typical neritic facies.

As previously mentioned, the lithological characteristics and sedimentary features, including the grain size, detrital minerals, and foraminifer, vary abruptly at 28 cm with an age of 9.6 kyr (**Figures 2**, **4**). Similarly, obvious variations in the grain size and magnetic qualities of the core YS01A in the west CYSM occur at 9.7 kyr as a result of strong erosion processes (Wang et al., 2014b). These indicate that the horizon of 28 cm represents a sedimentary hiatus in H10, and the erosion may widely exist in the CYSM during the early Holocene. Moreover, the sediment type and measured indexes of grain size and minerals at 103 cm shift abruptly (**Figures 2**, **4**), probably indicating that another erosional hiatus occurred at ~25 kyr.

4.3 Sedimentary Evolution Since MIS3a

According to the AMS ^{14}C ages (**Figure 2A**) and the variation in the oxygen isotopes of the planktonic *Foraminifera* in the Okinawa Trough, East China Sea (**Figure 8B**; Liu et al., 1999), DU3, DU2, and DU1 approximately correspond to MIS3a (late MIS3), MIS2, and MIS1 (Rasmussen and Thomsen, 2013), respectively. In this section, the sedimentary evolution of the study area and their responses to changes in RSL and climate, pathways of sediment supplies, and hydrodynamic regimes are discussed.

4.3.1 MIS3a (45–25 kyr)

Though it was interrupted by many millennium events of Heinrich and Dansgaard–Oeschger (D–O), MIS3a was a sub-interglacial in the last glacial period, displaying a relatively warm period (Shi et al., 2001; Yang et al., 2004; Wang et al., 2008) and was characterized by the fluctuating fall of RSL from 40 to 80 m bpsl (**Figure 8A**; Linsley, 1996; Shackleton, 2000). At this time, the east edge of the CYSM twice experienced facies shifts from neritic sea to shore, which are approximately proved by two cycles of increase to decrease of grain size, authigenic pyrite, and *Foraminifera* (**Figure 2**). Under the background of frequent RSL changes, the SR was lower than 8 cm/ka owing to the resuspension function and erosion activity induced by powerful tidal currents (Hanebuth et al., 2003; Hanebuth and Lantzsch, 2008). In this stage, the paleo-Yellow River carried a large number of sediments into the western SYS and formed a large delta, which in turn, developed an incised channel system in the late MIS3 with the delta likely advancing toward the sea (**Figure 9A**; Liu et al., 2010a). Meanwhile, dominated by the paleo-Yangtze River, a large well-developed coastal plain–delta complex was formed on the inner shelf and middle East China Sea (**Figure 9A**; Saito et al., 1998; Wellner and Bartek, 2003; Sun et al., 2014). The sediment provenance at the east edge of the CYSM was controlled by the paleo-Yellow River and, to some extent, influenced by the paleo-Yangtze River due to the shorter distance between the estuary and study area. Moreover, some horizons of DU3 are enriched authigenic pyrite and fine sediments (**Figures 2C,E**). Authigenic pyrite is a convenient proxy for indicating the existence of paleo-cold water mass and a

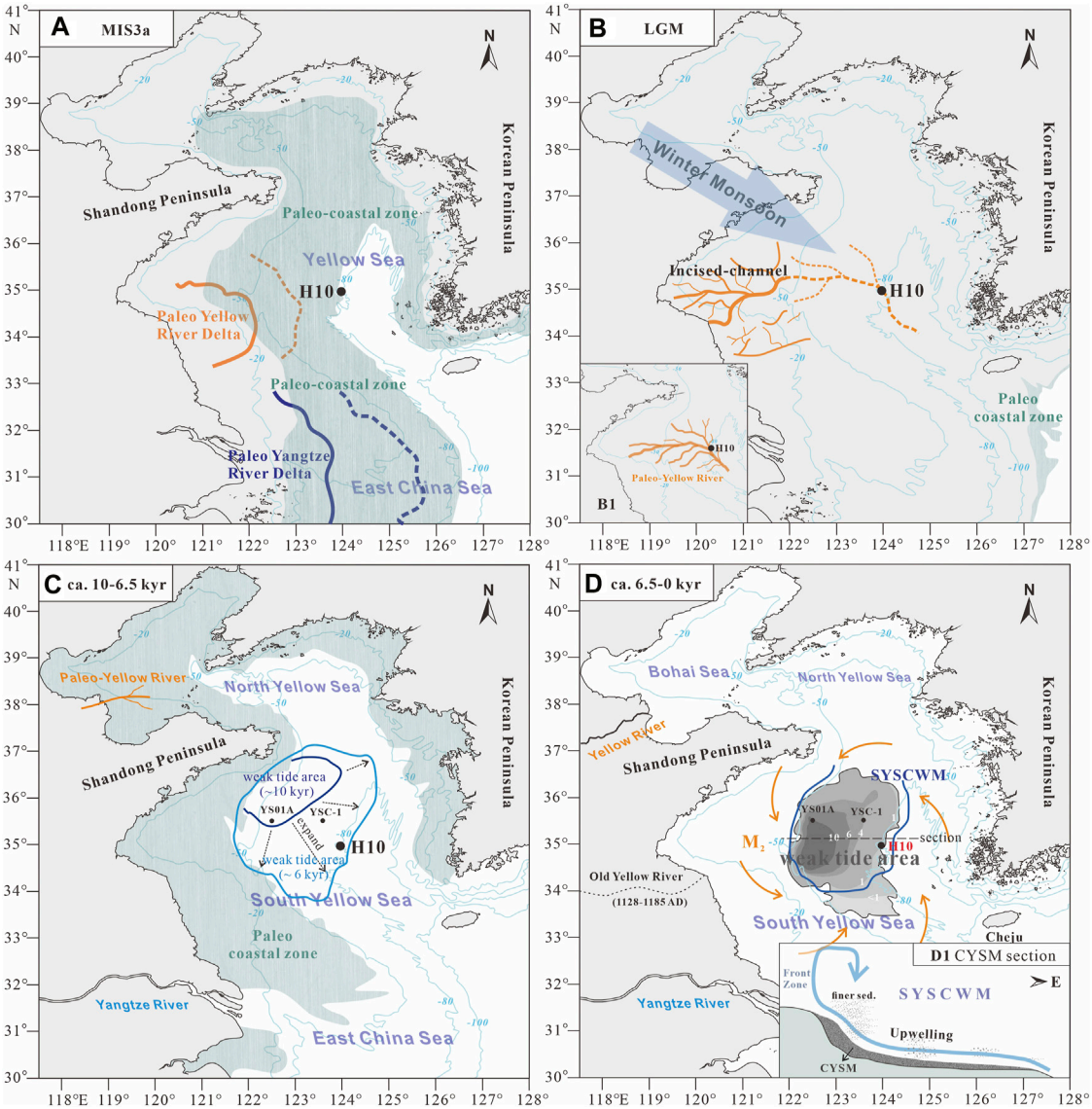

FIGURE 9 | Schematic diagrams for variation of coastal lines (Li et al., 2014a), distribution of paleo-rivers (Liu et al., 2002; Wellner and Bartek, 2003; Liu et al., 2010a; Song et al., 2016), evolution of hydrodynamic regimes (Uehara and Saito, 2003; Lü et al., 2010; Wang et al., 2014a), and formation of the CYSM (mud thickness is from Wang et al., 2014b) in the South Yellow Sea during MIS3a **(A)**, LGM **(B)**, ~10–6.5 kyr **(C)**, and 6.5 kyr—present **(D)**. The dotted line represents the inferred paths and ranges. The blue lines are all modern water depths. MIS, marine isotope stage; LGM, Last Glacial Maximum; CYSM, central Yellow Sea mud; SYSCWM, South Yellow Sea Cold Water Mass.

high sea-level period. However, its accumulation requires strict conditions, such as fine-grained sediments, weak hydrological dynamics, and a suitable redox environment (Chen, 2008). Consequently, the horizons that are enriched in authigenic pyrite likely correspond to high RSL periods with paleo-cold water mass and muddy deposition, which was not developed exclusively in the Holocene (Wang et al., 2014b; Mei et al., 2016). Conversely, horizons enriched with flake minerals, which are characteristic minerals of the Yellow River, may indicate that the paleo-Yellow River was close to the study area with a lower RSL (**Figure 4G**; Qin et al., 2018; Jin et al., 2019).

During the transition between MIS3a and MIS2, the RSL abruptly fell from 60 m bpsl to 110 m bpsl (**Figure 8A**), and a cold–dry event (Heinrich event 2) occurred at ~25 kyr (Rasmussen and Thomsen., 2013), which could have given rise to depositional stagnation and even the appearance of erosion present in the study area.

4.3.2 MIS2 to Early Holocene (25–10 kyr)

The RSL in the eastern China seas can be generally characterized by a rapid fall from 90 to 140 m bpsl, relative stabilization at 140 m bpsl, and a rapid rise from 140 to 60 m bpsl in the early

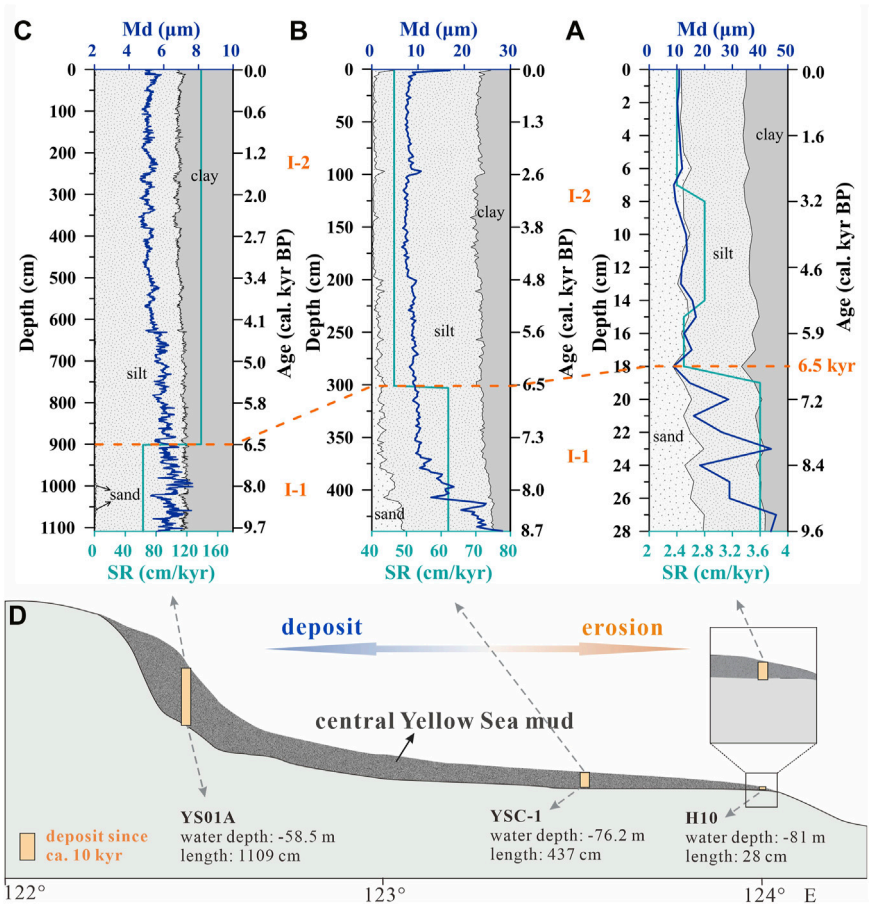

FIGURE 10 | Comparison of the sedimentary characteristics of core H10 **(A)**, YSC-1 (Hu et al., 2018) **(B)**, and YS01A (Wang et al., 2014b) **(C)** in the central Yellow Sea mud. **(D)** is a perspective transverse section of the central Yellow Sea mud.

MIS2, Last Glacial Maximum (LGM), and early last deglaciation, respectively (**Figure 8A**). In particular, the continental shelf of eastern China was completely exposed, and the paleo-coastal line occurred at the continental shelf edge of the East China Sea in LGM (**Figure 9B**; Lambeck and Chappell, 2001; Li et al., 2014a). The results of sediment provenance in the H10 core show intense Yellow River-derived features (**Figures 5–7**), and the caliche nodules usually form under the pedogenesis of fluvial sediments enriching terrestrial carbonate, while the content of $CaCO_3$ is higher in the Yellow River (Milliman et al., 1985; Milliman et al., 1987; Alexander et al., 1991). Consequently, our study area was likely located in one of the branches of the paleo-Yellow River's dendritic channel-network, which began to form in the western SYS in the late MIS3 (MIS3a) and probably extended east to the YST during LGM (**Figure 9B**; Liu et al., 2010a). Moreover, caliche nodules were also found in the west CYSM with some terricolous plant fragments during the MIS2 (Wang et al., 2014b), which further confirms that the dendritic channels of the paleo-Yellow River were widely distributed on the SYS. These results were also validated by Song et al. (2016) who used a more detailed network of seismic profiles that covered the area from 32°N to 36°N and 120°E to 125°E (**Figure 9B**). However, as influenced by the relatively cold and dry climate, sediment supplies from the paleo-Yellow River to the eastern continental shelf of China would be relatively low, and even eroded under the functions of transport and blowing by the winter monsoon (An et al., 1991). Furthermore, in this environment, there may be a disintegration of the previous marine strata, wherein marine materials may spread to the surrounding continental strata (Zhao et al., 1996), causing a few *Foraminifera*, authigenic pyrite, and glauconite to mix in the MIS2 strata.

During the transition from the late MIS2 to the early Holocene (~11.6–10 kyr), the Yellow River changed its route from the exposed shelf of the modern SYS to the Bohai Sea (Milliman et al., 1987; Liu et al., 2004; Liu et al., 2014b). This would have seriously reduced the fluvial discharge to the SYS, especially during the cold–dry events, such as the Younger Dryas during 12.9–11.6 kyr (Koutavas et al., 2002). Meanwhile, the rapid RSL rise to 45 m bpsl would facilitate erosion of the previous fluvial sediment in the study area with a stronger to-and-fro tidal current (Han et al., 2009). The limitation of sediment supplies to the SYS and the tidal erosion associated with the rapid RSL rise would be responsible for the hiatus that occurred in the study area between the late MIS2 and the early Holocene.

4.3.3 Sedimentary Evolution Since 9.6 kyr

In MIS1, the RSL has been steadily rising from 40 m bpsl at ~10 kyr, reached the present level at ~6.5 kyr, and finally has been stable to present (**Figure 8**). The east edge of the modern CYSM developed neritic facies, which was proven by the results of authigenic pyrite, authigenic glauconite, and *Foraminifera* (**Figures 2E–G**). The gradual increase of the grain size and authigenic glauconite from 28 to 18 cm and the relative stabilization from 18 to 0 cm in H10 (**Figures 2C,D,F**) indicate that the sedimentary environment at the east edge of the modern CYSM underwent a two-stage evolution bounded by 6.5 kyr (**Figures 9**, **10A**).

During Stage Ⅰ-1 (9.6–6.5 kyr) with RSL rising, the weak tidal area (<0.35 N/cm^2 stress intensity) extended from northwestern to southeastern SYS with the increase of amphidromic points (**Figure 9C**; Uehara and Saito, 2003). The upward-fining trend of grain size in the east edge of the CYSM responded to this phenomenon properly. The extremely low SR (3.3 cm/kyr) was caused under the strong hydrodynamic conditions (i.e., far away from the weak tidal area), which can be proven by the presence of less authigenic pyrite and *Foraminifera*, as well as high heavy mineral maturity and stable minerals content (**Figures 2**, **4**).

During Stage Ⅰ-2 (6.5 kyr to present), the RSL and tidal regimes reached the present level and were stable (Uehara and Saito, 2003; Zhou et al., 2015), which resulted in the relatively constant sediment composition in our region. In this period, the cold water mass in the central SYS (SYSCWM) occurred. With intense temperature stratification over the water column, the CWM can suppress turbulence development and restrain sediment resuspension (Dong et al., 2011; Wang et al., 2014a). However, the study area was located on the fringe of the SYSCWM and was likely reworked by upwelling and tidal currents (Gao and Jia, 2003; Lü et al., 2010). Therefore, the relatively strong hydrodynamic conditions induced by them resulted in the extremely low SR (2.4–3.1 cm/kyr) since 6.5 kyr. The presence of less authigenic pyrite and *Foraminifera*, as well as high heavy mineral maturity and stable minerals content demonstrated, are the best evidence under the strong hydrodynamic condition. The modern SR of the SYS calculated using ^{210}Pb also shows that the study area has an extremely low SR (Qiao et al., 2017).

The H10 core records the sedimentary evolution of the east edge of the CYSM since ~9.6 kyr, which closely approaches the initial time of the Holocene CYSM formation (Wang et al., 2014b; Xue et al., 2018). Combined with previously studied cores of YSC-1 in the central CYSM since 8.70 kyr and YS01A in the western CYSM since 9.7 kyr (**Figures 10A–C**; Hu et al., 2018; Wang et al., 2014b), a much more detailed and intuitional cognition of the CYSM formation processes and mechanisms can be achieved (**Figure 10D**). During 9.6–6.5 kyr, the weak tidal area gradually approached the scope of modern CYSM (**Figure 9C**; Uehara and Saito, 2003). Collectively and remarkably, the cores YSC-1 and H10 show the upward-fining trend in the grain size, whereas the core YS01A maintains a fine sediments deposit because its site was still in a weak tidal area. Therefore, the west of modern CYSM gradually became a depocenter with fine sediments, while the east edge of CYSM was more easily reworked by the tidal current with more Yellow River affinity coarser fractions remaining *in situ* (Qin et al., 2018). It is the westward enhancement of the net depositional effect that led to a significant increase in the SR from cores H10 to SYC-1, and then to YS01A during this period (**Figure 10**). Since 6.5 kyr, the sediments compositions in the CYSM were relatively constant due to the stable RSL and tidal regimes (**Figure 10**). The M_2 tidal current was attenuated toward the center of SYS in a convergent and anticlockwise pattern under the bottom friction and promotes an eddy circumfluence around the CYSM (**Figure 9D**; Zhou et al., 2015). Under the functions of sediment transport *via* tidal current and capture from the SYSCWM (Zhu and Chang, 2000; Uehara and Saito, 2003; Dong et al., 2011; Wang et al., 2014b), the CYSM became a fine-grained sedimentary body with multiple sources (Yang et al., 2003). Moreover, the upwelling induced by tidal mixing on the vertical circulation could rework pre-deposited sediments on the slope and move fine sediments upward, which leads to the maximum accumulation thickness in the frontal zone (Gao and Jia, 2003; Lü et al., 2010; Wang et al., 2014b). The cores of H10, SYC-1, and YS01A have 2.8, 46.4, and 138.5 cm/kyr in SR, and 11.9, 8.3, and 5.4 μm in the grain size, respectively (**Figure 10**). Therefore, this westward increase of SR and decrease of sediments grain size in the CYSM perfectly responded to the capture role of SYSCWM for fine sediments and shaped the role of upwelling for mud area formation.

5 CONCLUSION

Based on the grain size, heavy minerals, authigenic minerals, *Foraminifera*, end-member compositions of garnet, and caliche nodules in core H10, the sedimentary evolution at the east edge of the CYSM over the last ~45 kyr has been reconstructed. The provenance of coarser sediments of the core has remarkable Yellow River-derived characteristics, especially during MIS2 and MIS1, as determined using GS–HE and G–P–AS diagrams. The sedimentary evolution was primarily controlled by hydrodynamic regimes accompanied by changes in RSL and climate. During MIS3a, frequent RSL fluctuation was the predominant factor controlling two facies shifts from shallow sea to shore, and powerful tidal current erosion was responsible for a lower SR in the study area. The paleo-cold water mass and muddy deposition may occur in the high RSL stages with authigenic pyrite enrichment. The cold–dry event could result in the depositional stagnation and erosion present in the study area between MIS3a and MIS2. During MIS2, the paleo-Yellow River's dendritic channels were distributed on the SYS, flowed through the study area, and approached the YST in the LGM. Fluvial deposition on the shelf was eroded as a result of strong winter monsoon under the background of an extremely dry and cold climate. The limited sediment supply and tidal erosion associated with the rapid RSL rise could be responsible for the appearance of a sedimentary hiatus in the SYS between the late MIS2 and early Holocene. Since ~9.6 kyr, intense hydrodynamic regimes were responsible for the very thin deposition, and meanwhile, coarser sediments remained in the study area. Specifically, our study area was

impacted by expanding the weak tidal area during 9.6–6.5 kyr, as well as upwelling and tidal current after 6.5 kyr. Notably, combined with previously studied cores, a much more detailed and intuitional cognition of the CYSM formation processes and mechanisms were achieved from our special perspective: mud periphery.

DATA AVAILABILITY STATEMENT

The original contributions presented in the study are included in the article/**Supplementary Material**; further inquiries can be directed to the corresponding authors.

AUTHOR CONTRIBUTIONS

YZ contributed to laboratory analysis, data analysis, and manuscript writing. XM, ZH, and BJ contributed to project design and method establishment. ZL and JL contributed to field investigation and laboratory analysis. All authors have reviewed the manuscript.

FUNDING

This work was financially supported by the National Natural Science Foundation of China (NSFC, Grant No. U1606401) and the Basic Scientific Fund for National Public Research Institutes of China (No. 2021Q04).

ACKNOWLEDGMENTS

We are grateful to Dr. Yonghong Wang from the Ocean University of China and Dr. Bangqi Hu from the Qingdao Institute of Marine Geology, China Geological Survey, for providing the raw data of cores YS01A and YSC-1.

SUPPLEMENTARY MATERIAL

The Supplementary Material for this article can be found online at: https://www.frontiersin.org/articles/10.3389/feart.2022.889268/full#supplementary-material

REFERENCES

Alexander, C. R., DeMaster, D. J., and Nittrouer, C. A. (1991). Sediment Accumulation in a Modern Epicontinental-Shelf Setting: The Yellow Sea. *Mar. Geol.* 98, 51–72. doi:10.1016/0025-3227(91)90035-3

An, Z., Kukla, G. J., Porter, S. C., and Xiao, J. (1991). Magnetic Susceptibility Evidence of Monsoon Variation on the Loess Plateau of Central China during the Last 130,000 Years. *Quat. Res.* 36, 29–36. doi:10.1016/0033-5894(91)90015-w

Chen, L. R. (2008). *Sedimentary Mineralogy of the China Sea*. Beijing: China Ocean Press, 335–412. (in Chinese).

Cho, Y.-G., Lee, C.-B., and Choi, M.-S. (1999). Geochemistry of Surface Sediments off the Southern and Western Coasts of Korea. *Mar. Geol.* 159, 111–129. doi:10.1016/s0025-3227(98)00194-7

Dong, L. X., Guan, W. B., Chen, Q., Li, X. H., Liu, X. H., and Zeng, X. M. (2011). Sediment Transport in the Yellow Sea and East China Sea. *Estuar. Coast. Shelf Sci.* 93, 248–258. doi:10.1016/j.ecss.2011.04.003

Galehouse, J. S. (1971). "Sedimentation Analysis," in *Procedures in Sedimentary Petrology*. Editor R. E. Carver (New York: Wiley), 385–407.

Gao, S., and Collins, M. B. (2014). Holocene Sedimentary Systems on Continental Shelves. *Mar. Geol.* 352, 268–294. doi:10.1016/j.margeo.2014.03.021

Gao, S., and Jia, J.-j. (2003). Modeling Suspended Sediment Distribution in Continental Shelf Upwelling/downwelling Settings. *Geo-Mar Lett.* 22, 218–226. doi:10.1007/s00367-002-0116-8

Garzanti, E., Andò, S., and Vezzoli, G. (2008). Settling Equivalence of Detrital Minerals and Grain-Size Dependence of Sediment Composition. *Earth Planet. Sci. Lett.* 273, 138–151. doi:10.1016/j.epsl.2008.06.020

Grew, E. S., Locock, A. J., Mills, S. J., Galuskina, I. O., Galuskin, E. V., and Halenius, U. (2013). Nomenclature of the Garnet Supergroup. *Am. Mineralogist* 98, 785–811. doi:10.2138/am.2013.4201

Han, X., Shi, J., Li, J., and Li, G. (2009). Dynamical Simulation on Tidal Current Field in Ancient Yellow Sea during Younger Dryas Episode. *Mar. Geol. Quat. Geol.* 29, 13–24. (In Chinese with English abstract). doi:10.3724/sp.j.1140.2009.01013

Hanebuth, T. J. J., and Lantzsch, H. (2008). A Late Quaternary Sedimentary Shelf System under Hyperarid Conditions: Unravelling Climatic, Oceanographic and Sea-Level Controls (Golfe d'Arguin, Mauritania, NW Africa). *Mar. Geol.* 256, 77–89. doi:10.1016/j.margeo.2008.10.001

Hanebuth, T. J. J., Stattegger, K., Schimanski, A., Lüdmann, T., and Wong, H. K. (2003). Late Pleistocene Forced-Regressive Deposits on the Sunda Shelf (Southeast Asia). *Mar. Geol.* 199, 139–157. doi:10.1016/s0025-3227(03)00129-4

He, X. B., Tang, K. L., and Lei, X. Y. (1997). Heavy Mineral Record of the Holocene Environment on the Loess Plateau in China and its Pedogenetic Significance. *Catena* 29, 323–332. doi:10.1016/S0341-8162(96)00073-2

Hu, B., Li, J., Zhao, J., Yan, H., Zou, L., Bai, F., et al. (2018). Sr-Nd Isotopic Geochemistry of Holocene Sediments from the South Yellow Sea: Implications for Provenance and Monsoon Variability. *Chem. Geol.* 479, 102–112. doi:10.1016/j.chemgeo.2017.12.033

Huang, J., Wan, S., Zhang, J., Liu, J., Mei, X., Hu, B., et al. (2019). Mineralogical and Isotopic Evidence for the Sediment Provenance of the Western South Yellow Sea since MIS 3 and Implications for Paleoenvironmental Evolution. *Mar. Geol.* 414, 103–117. doi:10.1016/j.margeo.2019.05.011

Jin, B. F., Wang, M. Y., Yue, W., Zhang, L. N., and Wang, Y. J. (2019). Heavy Mineral Variability in the Yellow River Sediments as Determined by the Multiple–Window Strategy. *Minerals* 85, 2–16. doi:10.3390/min9020085

Keith, M. L., and Weber, J. N. (1964). Carbon and Oxygen Isotopic Composition of Selected Limestones and Fossils. *Geochimica Cosmochimica Acta* 28, 1787–1816. doi:10.1016/0016-7037(64)90022-5

Koutavas, A., Lynch-Stieglitz, J., Marchitto, T. M., and Sachs, J. P. (2002). El Niño-like Pattern in Ice Age Tropical Pacific Sea Surface Temperature. *Science* 297, 226–230. doi:10.1126/science.1072376

Krippner, A., Meinhold, G., Morton, A. C., and von Eynatten, H. (2014). Evaluation of Garnet Discrimination Diagrams Using Geochemical Data of Garnets Derived from Various Host Rocks. *Sediment. Geol.* 306, 36–52. doi:10.1016/j.sedgeo.2014.03.004

Lambeck, K., and Chappell, J. (2001). Sea Level Change through the Last Glacial Cycle. *Science* 292, 679–686. doi:10.1126/science.1059549

Li, G., Li, P., Liu, Y., Qiao, L., Ma, Y., Xu, J., et al. (2014a). Sedimentary System Response to the Global Sea Level Change in the East China Seas since the Last Glacial Maximum. *Earth-Science Rev.* 139, 390–405. doi:10.1016/j.earscirev.2014.09.007

Li, G., Qiao, L., Dong, P., Ma, Y., Xu, J., Liu, S., et al. (2016). Hydrodynamic Condition and Suspended Sediment Diffusion in the Yellow Sea and East China Sea. *J. Geophys. Res. Oceans* 121, 6204–6222. doi:10.1002/2015jc011442

Li, J., Hu, B., Wei, H., Zhao, J., Zou, L., Bai, F., et al. (2014b). Provenance Variations in the Holocene Deposits from the Southern Yellow Sea: Clay Mineralogy Evidence. *Cont. Shelf Res.* 90, 41–51. doi:10.1016/j.csr.2014.05.001

Lim, D., Xu, Z., Choi, J., Li, T., and Kim, S. (2015). Holocene Changes in Detrital Sediment Supply to the Eastern Part of the Central Yellow Sea and Their Forcing Mechanisms. *J. Asian Earth Sci.* 105, 18–31. doi:10.1016/j.jseaes.2015.03.032

Linsley, B. K. (1996). Oxygen-isotope Record of Sea Level and Climate Variations in the Sulu Sea over the Past 150,000 Years. *Nature* 380, 234–237. doi:10.1038/380234a0

Liu, J. P., Milliman, J. D., Gao, S., and Cheng, P. (2004). Holocene Development of the Yellow River's Subaqueous Delta, North Yellow Sea. *Mar. Geol.* 209, 45–67. doi:10.1016/j.margeo.2004.06.009

Liu, J. Q., Liu, Y. L., Yin, P., Gao, F., Cao, K., and Chen, X. Y. (2022). Composition, Source and Environmental Indication of Clay Minerals in Sediments from Mud Deposits in the Southern Weihai Offshore, Northwestern Shelf of the South Yellow Sea, China. *J. Ocean Univ. China* 21 (5), 1–13. doi:10.1007/s11802-022-4863

Liu, J. P., Milliman, J. D., and Gao, S. (2002). The Shandong Mud Wedge and Post-glacial Sediment Accumulation in the Yellow Sea. *Geo-Mar Lett.* 21, 212–218. doi:10.1007/s00367-001-0083-5

Liu, J., Saito, Y., Kong, X., Wang, H., Wen, C., Yang, Z., et al. (2010a). Delta Development and Channel Incision during Marine Isotope Stages 3 and 2 in the Western South Yellow Sea. *Mar. Geol.* 278, 54–76. doi:10.1016/j.margeo.2010.09.003

Liu, J., Shi, X., Liu, Q., Ge, S., Liu, Y., Yao, Z., et al. (2014a). Magnetostratigraphy of a Greigite-Bearing Core from the South Yellow Sea: Implications for Remagnetization and Sedimentation. *J. Geophys. Res. Solid Earth* 119, 7425–7441. doi:10.1002/2014jb011206

Liu, J., Yin, P., Zhang, Y., Song, H., Bi, S., Cao, Z., et al. (2017). Distribution and Provenance of Detrital Minerals in Southern Coast of Shandong Peninsula. *J. Ocean. Univ. China* 16, 747–756. doi:10.1007/s11802-017-3196-9

Liu, P. H., Liu, F. L., Wang, F., and Liu, J. H. (2010b). Genetic Mineralogy and Metamorphic Evolution of Mafic High–Pressure (HP) Granulites from the Shandong Peninsula, China. *Acta Petrol. Sin.* 26, 2039–2056. (in Chinese with English abstract). doi:10.1016/j.sedgeo.2010.06.006

Liu, S., Feng, A., Du, J., Xia, D., Li, P., Xue, Z., et al. (2014b). Evolution of the Buried Channel Systems under the Modern Yellow River Delta since the Last Glacial Maximum. *Quat. Int.* 349, 327–338. doi:10.1016/j.quaint.2014.06.061

Liu, Z., Saito, Y., Li, T., Berne, S., Chen, Z., Li, P., et al. (1999). Millennial-scale Paleoceanography in Okinawa Trough during Late Quaternary Period. *Chin. Sci. Bull.* 44, 1705–1709. doi:10.1007/bf03183496

Lü, X. G., Qiao, F. L., Xia, C. S., Wang, G. S., and Yuan, Y. L. (2010). Upwelling and Surface Cold Patches in the Yellow Sea in Summer: Effects of Tidal Mixing on the Vertical Circulation. *Cont. Shelf Res.* 30, 620–632. doi:10.1016/j.csr.2009.09.002

Mange, M. A., and Maurer, H. F. W. (1992). *Heavy Minerals in Colour*. London: Chapman & Hall, 1–34.

Mange, M. A., and Morton, A. C. (2007). "Chapter 13 Geochemistry of Heavy Minerals," in *Heavy Minerals in Use*. Editors M. Mange and D. K. Wright (Amsterdam: Elsevier), 345–391. doi:10.1016/s0070-4571(07)58013-1

Mei, X., Li, R., Zhang, X., Liu, Q., Liu, J., Wang, Z., et al. (2016). Evolution of the Yellow Sea Warm Current and the Yellow Sea Cold Water Mass since the Middle Pleistocene. *Palaeogeogr. Palaeoclimatol. Palaeoecol.* 442, 48–60. doi:10.1016/j.palaeo.2015.11.018

Milliman, J. D., Beardsley, R. C., Zuo-sheng, Y., and Limeburner, R. (1985). Modern Huanghe-Derived Muds on the Outer Shelf of the East China Sea: Identification and Potential Transport Mechanisms. *Cont. Shelf Res.* 4, 175–188. doi:10.1016/0278-4343(85)90028-7

Milliman, J. D., Yun-Shan, Q., Mei-E, R., and Saito, Y. (1987). Man's Influence on the Erosion and Transport of Sediment by Asian Rivers: The Yellow River (Huanghe) Example. *J. Geol.* 95, 751–762. doi:10.1086/629175

Morton, A. C. (1985). A New Approach to Provenance Studies: Electron Microprobe Analysis of Detrital Garnets from Middle Jurassic Sandstones of the Northern North Sea. *Sedimentology* 32, 553–566. doi:10.1111/j.1365-3091.1985.tb00470.x

Morton, A. C., and Hallsworth, C. (1994). Identifying Provenance-specific Features of Detrital Heavy Mineral Assemblages in Sandstones. *Sediment. Geol.* 90, 241–256. doi:10.1016/0037-0738(94)90041-8

Morton, A. C., and Hallsworth, C. R. (1999). Processes Controlling the Composition of Heavy Mineral Assemblages in Sandstones. *Sediment. Geol.* 124, 3–29. doi:10.1016/s0037-0738(98)00118-3

Morton, A. C. (1987). Influences of Provenance and Diagenesis on Detrital Garnet Suites in the Forties Sandstone, Paleocene, Central North Sea. *J. Sediment. Petrology* 57, 1027–1032. doi:10.1306/212f8cd8-2b24-11d7-8648000102c1865d

Morton, A., Hallsworth, C., and Chalton, B. (2004). Garnet Compositions in Scottish and Norwegian Basement Terrains: a Framework for Interpretation of North Sea Sandstone Provenance. *Mar. Petroleum Geol.* 21, 393–410. doi:10.1016/j.marpetgeo.2004.01.001

Park, S.-C., Lee, H.-H., Han, H.-S., Lee, G.-H., Kim, D.-C., and Yoo, D.-G. (2000). Evolution of Late Quaternary Mud Deposits and Recent Sediment Budget in the Southeastern Yellow Sea. *Mar. Geol.* 170, 271–288. doi:10.1016/s0025-3227(00)00099-2

Qiao, S., Shi, X., Wang, G., Zhou, L., Hu, B., Hu, L., et al. (2017). Sediment Accumulation and Budget in the Bohai Sea, Yellow Sea and East China Sea. *Mar. Geol.* 390, 270–281. doi:10.1016/j.margeo.2017.06.004

Qin, Y.-C., Xue, C., and Jiang, X. (2018). Tidal Current-Dominated Depositional Environments in the Central-Northern Yellow Sea as Revealed by Heavy-Mineral and Grain-Size Dispersals. *Mar. Geol.* 398, 59–72. doi:10.1016/j.margeo.2018.01.004

Qin, Y. S., Zhao, Y. Y., Chen, L. R., and Zhao, S. L. (1989). *Geology of the Yellow Sea*. Beijing: China Ocean Press, 1–24. (in Chinese).

Rasmussen, T. L., and Thomsen, E. (2013). Pink Marine Sediments Reveal Rapid Ice Melt and Arctic Meltwater Discharge during Dansgaard-Oeschger Warmings. *Nat. Commun.* 4, 2849. doi:10.1038/ncomms3849

Reimer, P. J., Bard, E., Bayliss, A., Beck, J. W., Blackwell, P. G., Ramsey, C. B., et al. (2013). IntCal13 and Marine13 Radiocarbon Age Calibration Curves 0-50,000 Years Cal BP. *Radiocarbon* 55, 1869–1887. doi:10.2458/azu_js_rc.55.16947

Ren, M.-E., and Shi, Y.-L. (1986). Sediment Discharge of the Yellow River (China) and its Effect on the Sedimentation of the Bohai and the Yellow Sea. *Cont. Shelf Res.* 6, 785–810. doi:10.1016/0278-4343(86)90037-3

Sabeen, H. M., Ramanujam, N., and Morton, A. C. (2002). The Provenance of Garnet: Constraints provided by Studies of Coastal Sediments from Southern India. *Sediment. Geol.* 152, 279–287. doi:10.1016/s0037-0738(02)00083-0

Saito, Y., Katayama, H., Ikehara, K., Kato, Y., Matsumoto, E., Oguri, K., et al. (1998). Transgressive and Highstand Systems Tracts and Post-glacial Transgression, the East China Sea. *Sediment. Geol.* 122, 217–232. doi:10.1016/s0037-0738(98)00107-9

Sevastjanova, I., Hall, R., and Alderton, D. (2012). A Detrital Heavy Mineral Viewpoint on Sediment Provenance and Tropical Weathering in SE Asia. *Sediment. Geol.* 280, 179–194. doi:10.1016/j.sedgeo.2012.03.007

Shackleton, N. J. (2000). The 100,000-year Ice-Age Cycle Identified and Found to Lag Temperature, Carbon Dioxide, and Orbital Eccentricity. *Science* 289, 1897–1902. doi:10.1126/science.289.5486.1897

Shi, X. F., Liu, Y. G., Chen, Z. H., Wei, J. W., Ge, S. L., Wang, K. S., et al. (2012). "Origin, Transport Processes and Distribution Pattern of Modern Sediments in the Yellow Sea," in *Sediments, Morphology and Sedimentary Processes on Continental Shelves-Advances in Technologies, Research and Applications*. Editors M. Z. Li, C. R. Sherwood, and P. R. Hill (Wiley), 321–350.

Shi, Y., Yu, G., Liu, X., Li, B., and Yao, T. (2001). Reconstruction of the 30-40 Ka Bp Enhanced Indian Monsoon Climate Based on Geological Records from the Tibetan Plateau. *Palaeogeogr. Palaeoclimatol. Palaeoecol.* 169, 69–83. doi:10.1016/s0031-0182(01)00216-4

Song, Z. J., Li, J. P., Gu, Z. K., Tang, W. J., Yu, J. F., and Gao, L. (2016). Characteristics of Buried Paleo–Channels in the Western South Yellow Sea during the Late Last Glaciation. *Teh. Vjesnik–Technical Gaz.* 23, 835–842. doi:10.17559/tv-20160216023828

Sun, Z., Li, G., and Yin, Y. (2014). The Yangtze River Deposition in Southern Yellow Sea during Marine Oxygen Isotope Stage 3 and its Implications for Sea–Level Changes. *Quat. Res.* 83, 204–215. doi:10.1016/j.yqres.2014.08.008

Takeuchi, M., Kawai, M., and Matsuzawa, N. (2008). Detrital Garnet and Chromian Spinel Chemistry of Permian Clastics in the Renge Area, Central Japan: Implications for the Paleogeography of the East Asian Continental Margin. *Sediment. Geol.* 212, 25–39. doi:10.1016/j.sedgeo.2008.09.002

Uehara, K., and Saito, Y. (2003). Late Quaternary Evolution of the Yellow/East China Sea Tidal Regime and its Impacts on Sediments Dispersal and Seafloor Morphology. *Sediment. Geol.* 162, 25–38. doi:10.1016/s0037-0738(03)00234-3

Wang, B., Hirose, N., Kang, B., and Takayama, K. (2014a). Seasonal Migration of the Yellow Sea Bottom Cold Water. *J. Geophys. Res. Oceans* 119, 4430–4443. doi:10.1002/2014jc009873

Wang, K. S., Wang, G. Q., Cai, S. W., Dou, Y. G., Shi, X. F., Cheng, Z. B., et al. (2007). Heavy Mineral Characteristics of Surface Sediments in the Subaqueous

Yangtze River Delta. *Mar. Geol. Quat. Geol.* 27, 7–12. (in Chinese with English abstract).

Wang, Y., Cheng, H., Edwards, R. L., Kong, X., Shao, X., Chen, S., et al. (2008). Millennial- and Orbital-Scale Changes in the East Asian Monsoon over the Past 224,000 Years. *Nature* 451, 1090–1093. doi:10.1038/nature06692

Wang, Y., Li, G., Zhang, W., and Dong, P. (2014b). Sedimentary Environment and Formation Mechanism of the Mud Deposit in the Central South Yellow Sea during the Past 40kyr. *Mar. Geol.* 347, 123–135. doi:10.1016/j.margeo.2013.11.008

Wang, Z. B. (2014). *The Late Quaternary Stratigraphy on the Outer Shelf of the East China Sea and its Provenance–Paleoenvironmental Study (Doctoral Thesis)*. Shanghai: Tongji University. (in Chinese).

Wellner, R. W., and Bartek, L. R. (2003). The Effect of Sea Level, Climate, and Shelf Physiography on the Development of Incised-Valley Complexes: A Modern Example from the East China Sea. *J. Sediment. Res.* 73, 926–940. doi:10.1306/041603730926

Xiang, R., Yang, Z., Saito, Y., Fan, D., Chen, M., Guo, Z., et al. (2008). Paleoenvironmental Changes during the Last 8400 Years in the Southern Yellow Sea: Benthic Foraminiferal and Stable Isotopic Evidence. *Mar. Micropaleontol.* 67, 104–119. doi:10.1016/j.marmicro.2007.11.002

Xue, C., Qin, Y., Ye, S., Laws, E. A., and Wang, Z. (2018). Evolution of Holocene Ebb-Tidal Clinoform off the Shandong Peninsula on East China Sea Shelf. *Earth-Science Rev.* 177, 478–496. doi:10.1016/j.earscirev.2017.12.012

Yang, B., Shi, Y., Braeuning, A., and Wang, J. (2004). Evidence for a Warm-Humid Climate in Arid Northwestern China during 40?30ka BP. *Quat. Sci. Rev.* 23, 2537–2548. doi:10.1016/j.quascirev.2004.06.010

Yang, S. Y., Jung, H. S., Lim, D. I., and Li, C. X. (2003). A Review on the Provenance Discrimination of Sediments in the Yellow Sea. *Earth-Science Rev.* 63, 93–120. doi:10.1016/s0012-8252(03)00033-3

Yang, S., and Youn, J.-S. (2007). Geochemical Compositions and Provenance Discrimination of the Central South Yellow Sea Sediments. *Mar. Geol.* 243, 229–241. doi:10.1016/j.margeo.2007.05.001

Yang, Z. S., and Liu, J. P. (2007). A Unique Yellow River-Derived Distal Subaqueous Delta in the Yellow Sea. *Mar. Geol.* 240, 169–176. doi:10.1016/j.margeo.2007.02.008

Yang, Z. S. (1988). Mineralogical Assemblages and Chemical Characteristics of Clays in from the Huanghe, Changjiang, and Zhujiang Rivers and Their Relationship to the Climate Environment in Their Source Areas. *Oceanol. Limnologia Sinica* 19, 336–346. (In Chinese with English abstract).

Zhao, S. L., Yu, H. J., and Liu, J. P. (1996). Discussion on the Environment Evolution Pattern of the Continental Shelf Desertification in the Late Pleistocene. *Sci. China* 26, 142–146. (in Chinese with English abstract).

Zhou, C., Dong, P., and Li, G. (2015). Hydrodynamic Processes and Their Impacts on the Mud Deposit in the Southern Yellow Sea. *Mar. Geol.* 360, 1–16. doi:10.1016/j.margeo.2014.11.012

Zhu, Y., and Chang, R. (2000). Preliminary Study of the Dynamic Origin of the Distribution Pattern of Bottom Sediments on the Continental Shelves of the Bohai Sea, Yellow Sea and East China Sea. *Estuar. Coast. Shelf Sci.* 51, 663–680. doi:10.1006/ecss.2000.0696

Zhuang, L. H., Chang, F. M., Li, T. G., and Yan, J. (2002). Foraminiferal Faunas and Holocene Sedimentation Rates of Core EY02-2 in the South Yellow Sea. *Mar. Geol. Quat. Geol.* 22, 7–14. (in Chinese with English abstract).

Conflict of Interest: The authors declare that the research was conducted in the absence of any commercial or financial relationships that could be construed as a potential conflict of interest.

Publisher's Note: All claims expressed in this article are solely those of the authors and do not necessarily represent those of their affiliated organizations, or those of the publisher, the editors, and the reviewers. Any product that may be evaluated in this article, or claim that may be made by its manufacturer, is not guaranteed or endorsed by the publisher.